










## Article

# Coated Biodegradable Zinc Lithium Alloys: Development and Characterization of Co-Doped Strontium Copper Tricalcium Phosphate Coating for Antimicrobial Applications

Julietta V. Rau <sup>1,2,\*</sup> , Angela De Bonis <sup>3</sup> , Mariangela Curcio <sup>3</sup> , Katia Barbaro <sup>4</sup> , Marco Fosca <sup>1</sup> ,  
Inna V. Fadeeva <sup>5</sup> , Giovana Collombaro Cardoso <sup>6</sup> , Roberto Teghil <sup>3</sup> , Tatiana K. Slonskaya <sup>2</sup>  
and Yufeng Zheng <sup>7</sup> 

- <sup>1</sup> Istituto di Struttura della Materia, Consiglio Nazionale delle Ricerche (ISM-CNR), Via del Fosso del Cavaliere 100, 00133 Rome, Italy; marco.fosca@ism.cnr.it
  - <sup>2</sup> Department of Analytical, Physical and Colloid Chemistry, Institute of Pharmacy, I.M. Sechenov First Moscow State Medical University, Trubetskaya 8, Build. 2, Moscow 119048, Russia; slonskaya\_t\_k@staff.sechenov.ru
  - <sup>3</sup> Dipartimento di Scienze, Università della Basilicata, Via dell'Ateneo Lucano 10, 85100 Potenza, Italy; angela.debonis@unibas.it (A.D.B.); curcio.mariangela@gmail.com (M.C.); roberto.teghil@unibas.it (R.T.)
  - <sup>4</sup> Istituto Zooprofilattico Sperimentale Lazio e Toscana "M. Aleandri", Via Appia Nuova, 00178 Rome, Italy; katia.barbaro@izslt.it
  - <sup>5</sup> A.A. Baikov Institute of Metallurgy and Material Science, Russian Academy of Sciences, Leninsky 49, Moscow 119334, Russia; fadeeva\_inna@mail.ru
  - <sup>6</sup> Laboratório de Anelasticidade e Biomateriais, UNESP—Universidade Estadual Paulista, Bauru 17033-360, SP, Brazil; giovana.collombaro@unesp.br
  - <sup>7</sup> School of Materials Science and Engineering, Peking University, No. 5 Yi-He-Yuan Road, Hai-Dian District, Beijing 100871, China; yfzheng@pku.edu.cn
- \* Correspondence: giulietta.rau@ism.cnr.it



**Citation:** Rau, J.V.; De Bonis, A.; Curcio, M.; Barbaro, K.; Fosca, M.; Fadeeva, I.V.; Cardoso, G.C.; Teghil, R.; Slonskaya, T.K.; Zheng, Y. Coated Biodegradable Zinc Lithium Alloys: Development and Characterization of Co-Doped Strontium Copper Tricalcium Phosphate Coating for Antimicrobial Applications. *Coatings* **2024**, *14*, 1073. <https://doi.org/10.3390/coatings14081073>

Academic Editor: Daniela Predoi

Received: 25 July 2024

Revised: 14 August 2024

Accepted: 20 August 2024

Published: 22 August 2024



**Copyright:** © 2024 by the authors. Licensee MDPI, Basel, Switzerland. This article is an open access article distributed under the terms and conditions of the Creative Commons Attribution (CC BY) license (<https://creativecommons.org/licenses/by/4.0/>).

**Abstract:** Zinc biodegradable implants represent a revolutionary advancement in medical technology, offering a promising alternative to titanium and stainless-steel implants and avoiding the need for secondary surgeries for removal. In this study, we aimed to fulfil the clinical demand for biodegradable implant materials by applying a coating of double-doped strontium and copper resorbable tricalcium phosphate (SrCu-TCP) onto a zinc-lithium (Zn-Li) biodegradable alloy using the Pulsed Laser Deposition method. The coated surfaces were thoroughly characterized using X-ray Diffraction, Fourier Transform Infrared Spectroscopy, Atomic Force Microscopy, and Scanning Electron Microscopy coupled with Energy Dispersive X-ray. Microbiology experiments were conducted to assess the inhibitory effects on the growth of various bacteria strains, including gram-positive *Staphylococcus aureus* and *Enterococcus faecalis*, gram-negative *Pseudomonas aeruginosa* and *Escherichia coli*, as well as the fungus *Candida albicans*. The obtained results showed that the roughness of the Zn-Li alloy increased from  $91.8 \pm 29.4$  to  $651.0 \pm 179.5$  nm when coated with SrCu-TCP. The thickness of the coating ranged between 3–3.5  $\mu\text{m}$ . The inhibition of growth for all four bacteria strains and the fungus was in the range of 24–35% when cultured on SrCu-TCP coated Zn-Li samples. These findings suggest that the developed coatings are promising candidates for applications requiring inhibition of microorganisms.

**Keywords:** coatings; biodegradable coatings; tricalcium phosphate coatings; copper and strontium doped tricalcium phosphate; copper and strontium co-doped tricalcium phosphate; biodegradable alloys; Zn-Li alloy

## 1. Introduction

In the past two decades, biodegradable metals have emerged as promising materials for various biomedical implant devices, offering the potential to reduce reliance on permanent metallic implants, such as those made of titanium (Ti) alloys, stainless steel, etc. [1–4].

This advancement aims to mitigate the need for implant removal surgeries and significantly decrease associated costs [5–8]. Biodegradable metals, including those used in bone implants, show advantages such as biocompatibility and controlled degradation [9–12]. However, challenges persist, including the need to address their excessive corrosion rates compared to the healing rate of host bone tissue and to provide implant surface with biomimetic properties [13–16].

Recent studies indicate that Zinc (Zn) is a crucial micronutrient for human health, particularly in bone tissue development and homeostasis [17–20]. It contributes to bone tissue composition, collagen synthesis, mineralization, and turnover [21–24]. Both in vitro and in vivo research demonstrate zinc's diverse effects: promoting osteoblast proliferation and differentiation while safeguarding osteoblasts from oxidative stress-induced apoptosis, and inhibiting osteoclastogenesis and impacting osteoclast apoptosis [25–27]. These properties, combined with its antibacterial activity, have led to successful utilization of zinc in bone substitutes and implant biomaterials [28]. The incorporation of zinc into various calcium phosphates like hydroxyapatite,  $\beta$ -TCP, brushite, or monetite holds promise as a beneficial agent in bone repair [29–31].

Binary Zn alloys with alloying elements such as magnesium (Mg), calcium (Ca), strontium (Sr), lithium (Li), manganese (Mn), iron (Fe), copper (Cu), and silver (Ag) are systemically investigated in vitro and in vivo. Li exhibits the most effective strengthening role in Zn, followed by Mg. Alloying leads to accelerated degradation. Adding elements such as Mg, Ca, Sr, and Li into Zn improves the cytocompatibility, osteogenesis, and osseointegration [32,33]. Li becomes toxic from 1.4 mM [34,35], and serum Li quantities are associated with bipolar disorders (10 mg/L) or risk of death (20 mg/L) [36,37]. However, in the quantities in which Li is included in implant alloys, it is not toxic [32,38]. Moreover, Li improved bone mass in mice and enhanced bone formation through the activation of the canonical Wnt pathway [39]. Additionally, maintenance therapy with lithium carbonate increased bone mass [40].

Coating biodegradable metal surfaces such as Mg-Ca [41–43] or Zn-Li alloys [44–46], with biomimetic calcium phosphates represents a significant strategy for enhancing their properties, including controlling degradation behaviour and improving surface biocompatibility. Tricalcium phosphate (TCP), particularly  $\beta$ -tricalcium phosphate ( $\beta$ -TCP), stands out as a resorbable bioceramic widely used in synthetic bone grafts due to its osteoconductive and osteoinductive properties [47]. To enhance  $\beta$ -TCP's osteoinductive ability, metal ions like  $\text{Sr}^{2+}$  [48],  $\text{Cu}^{2+}$  [49],  $\text{Mg}^{2+}$  [50],  $\text{Mn}^{2+}$  [51,52],  $\text{Fe}^{2+}$  [53], and  $\text{Zn}^{2+}$  [54] are incorporated, typically by substituting  $\text{Ca}^{2+}$  ions. These essential ions have been shown to enhance the biological performance of  $\beta$ -TCP, promoting osteo- and angiogenesis. Additionally, copper ( $\text{Cu}^{2+}$ ) [49], manganese ( $\text{Mn}^{2+}$ ) [51], iron ( $\text{Fe}^{2+}$ ) [53], and zinc ( $\text{Zn}^{2+}$ ) [54] exhibit antimicrobial properties, further bolstering the potential of these coatings in biomedical applications. In particular, copper is known to exert its antimicrobial effect by damaging the cell membrane and inducing the production of reactive oxygen species (ROS) that can, in turn, harm proteins, lipids, and DNA. Additionally, Cu can bind to bacterial enzymes, impairing their functions and preventing bacterial growth and replication [55,56].

Co-substituted  $\beta$ -TCP-based phosphates with  $\text{Cu}^{2+}/\text{Zn}^{2+}$ ,  $\text{Cu}^{2+}/\text{Sr}^{2+}$ , and  $\text{Sr}^{2+}/\text{Mn}^{2+}$  ion pairs were reported in [57]. In the same study, their antibacterial properties were evaluated. The results obtained demonstrated that all synthesized phases exhibit antibacterial effects. Notably, experiments using  $\beta$ -TCP-Cu+Sr, which had the highest concentration of  $\text{Cu}^{2+}$  ions among all samples studied and occupied separate crystal sites, showed minimal bacterial and fungal growth. It was concluded that the active dopant ions must be located in different crystal sites to provide higher antimicrobial activity.

It is important to highlight that implant-related infections continue to be a leading cause of implant failure, resulting in significant economic and social burdens [58,59]. Preventing biomaterial-associated infections requires targeted strategies aimed at inhibiting bacterial adhesion and biofilm formation. Alarming high rates of septic complications, particularly in high-risk patients and procedures, have been documented [60,61].

Microorganisms such as *Staphylococcus aureus* (*S. aureus*), *Pseudomonas aeruginosa* (*P. aeruginosa*), *Escherichia coli* (*E. coli*), *Enterococcus faecalis* (*E. faecalis*), and *Candida albicans* (*C. albicans*) are commonly found in hospital environments [62,63]. In particular, *S. aureus* is typically present on the skin and in the nostrils, posing a risk of contamination to surgical and medical instruments, and is a leading cause of nosocomial infections. *P. aeruginosa* is present in moist environments, such as sinks, antiseptic solutions, etc. *E. coli* and *E. faecalis* are primarily found in the intestinal and urinary tracts and can contaminate surgical surfaces and instruments. Meanwhile, *C. albicans* is frequently present on the skin and mucous membranes, also posing a contamination risk to medical instruments.

To render implant surfaces antibacterial and mitigate infection risks, coating them with materials possessing antibacterial properties is a viable approach. Among these materials are calcium phosphates substituted with ions, like copper (Cu), manganese (Mn), iron (Fe), and zinc (Zn).

In the present study, for the first time, Zn-Li biodegradable alloy was coated with double doped Sr and Cu resorbable tricalcium phosphate to address the clinical needs for biodegradable implant materials as an alternative to traditional titanium and stainless-steel implants. The alloy was coated by Pulsed Laser Deposition (PLD) to ensure a uniform and well-adhered coating, which is important for the performance and longevity of the implants. Coatings characterization was performed using X-ray Diffraction (XRD), Fourier Transform Infrared Spectroscopy (FTIR), Atomic Force Microscopy (AFM), and Scanning Electron Microscopy (SEM) coupled with Energy Dispersive X-ray (EDX). Microbiological tests were conducted on coated Zn-Li alloy samples, targeting gram-positive bacteria strains such as *S. aureus* and *E. faecalis* and gram-negative strains including *P. aeruginosa* and *E. coli*, as well as *C. albicans* fungus.

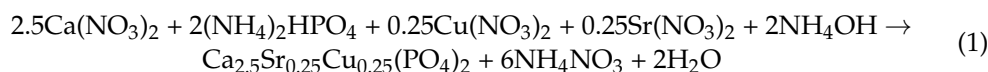
## 2. Materials and Methods

### 2.1. Zn-Li Alloy Preparation

Zn-0.4 wt% Li alloy was synthesized from a Zn (99.99%) and Zn-Li master alloy (6 wt% Li) ingot from the Hunan Rare Earth Metal Material Research Institute (Changsha, China). For casting, a cast iron mould with ZnO coating was applied. The obtained ingot was homogenized at 350 °C for 48 h, followed by water quenching. Then, it was deformed by hot extrusion at 260 °C with an extrusion ratio of 36:1 at 1 mm/s. The obtained samples were cut perpendicular to the extrusion direction, resulting in the following geometry: diameter of 10 mm and a thickness of 3 mm. All the prepared samples were ground to 2000 grit with SiC and then ultrasonically cleaned in acetone, absolute ethanol, and distilled water.

### 2.2. Synthesis of Bulk Target Material—Double Substituted Sr- and Cu- Tricalcium Phosphate (SrCu-TCP)

(Strontium and Copper)-containing TCP bulk material with formula  $\text{Ca}_{2.5}\text{Cu}_{0.25}\text{Sr}_{0.25}(\text{PO}_4)_2$  was synthesized using the method of mechanochemical activation. The weights of the initial reagents were calculated according to reaction (1):



To begin, 14.00 g CaO, 5.29 g  $\text{Sr}(\text{NO}_3)_2$ , 6.04 g  $\text{Cu}(\text{NO}_3)_2 \cdot 3\text{H}_2\text{O}$ , and 26.41 g  $(\text{NH}_4)_2\text{HPO}_4$  were placed into the Teflon container with 250 g zirconia balls and activation was carried out in a planetary mill (material: balls ratio of 1:3). The rotation speed was set at 200 rpm for 30 min, after which 200 mL of distilled water was added to the container and grinding was then continued for 30 min. Immediately after the grinding, the resulting precipitate was filtered out on a Buchner funnel and dried at 105 °C until completely dry. After that, the (copper and strontium)-substituted TCP was calcined at 400 °C for 1 h to remove the reaction by-products (ammonium nitrate and water). From the so-obtained powders, disks with a diameter of 15 mm were pressed by the method of uniaxial pressing at a specific

pressure of 200 kg/cm<sup>2</sup>. After that, the disks were sintered in a chamber furnace with silite heaters at 1200 °C for 2 h.

The weight% of Sr and Cu was calculated as follows:

$$\text{Ca}_{2.5}\text{Sr}_{0.25}\text{Cu}_{0.25}(\text{PO}_4)_2 \text{ M}_r = 2.5 \times 40.08 + 0.25 \times 87.62 + 0.25 \times 63.55 + (30.97 + 16.00 \times 4) \times 2 = 327.94 \quad (2)$$

$$\text{wt\% Sr} = 87.62 \times 0.25 \times 100/327.94 = 6.68 \quad (3)$$

$$\text{wt\% Cu} = 63.55 \times 0.25 \times 100/327.94 = 4.84 \quad (4)$$

The content of Sr and Cu in the prepared ceramic targets was determined using atomic absorption spectroscopy on an atomic absorption spectrometer (AAS) manufactured by Thermo Fisher Scientific (Madison, WI, USA), model iCE 3000.

### 2.3. Pulsed Laser Deposition of Coatings

For thin film deposition, the nanosecond PLD technique supplied with nanosecond Nd:YAG laser source ( $\lambda = 532$  nm, 10 Hz, 7 ns) was applied. SrCu-TCP discs of 1 cm diameter were applied as targets. The ablation and deposition experiments were carried out in a stainless-steel chamber equipped with a scroll-turbomolecular vacuum system. Films were grown on Zn-Li and monocrystalline Si(100), the latter being necessary for coatings' FTIR and XRD characterizations. Depositions were performed at a laser fluence of 12 J/cm<sup>2</sup> (250 mW) and a pressure of 10<sup>-4</sup> Pa for 2 h, with the target substrate distance fixed at 1 cm. The laser beam was incident at an angle of 45° on the target surface and focused by a 35 cm focus lens. All the films were deposited at room temperature of substrate. The disc target was fixed in a rotating holder in order to minimize the laser craterisation effect.

### 2.4. Physico-Chemical Characterization of Coatings

For XRD, a Siemens 5000D (Bruker, Billerica, MA, USA), operating at 40 kV and 32 mA and using CuK $\alpha$  radiation ( $\lambda = 1.5405600$  Å,  $2\theta = 10^\circ$ – $60^\circ$ , step size 0.040°, time per step 4 s), was employed.

FTIR spectra were acquired by a Jasco 460Plus interferometer (Jasco, Tokyo, Japan). For each sample, 100 spectra were collected at resolution of 4 cm<sup>-1</sup> in the 4000–400 cm<sup>-1</sup> range.

AFM measurements were performed using a Bruker Dimension Icon system equipped with a Nanoscope V controller. AFM images were acquired in tapping mode, using n-doped Si probes (Bruker RTESP300) with a resonant frequency of 300 kHz at a scan rate 0.3–1 Hz. The scanned areas were from 1 × 1 μm<sup>2</sup> to 10 × 10 μm<sup>2</sup>. Different regions were scanned for each sample.

Morphological characterization and cross-section were made by means of an FE-SEM (Auriga-Zeiss, Oberkochen, Germany) equipped with an EDS analyzer (Bruker).

### 2.5. Microbiology Tests

The antimicrobial activity of pure TCP and SrCu-TCP coatings on Zn-Li substrates was assessed. The samples were autoclaved at 121 °C for 20 min at a pressure of 1.1 bar and then immersed in BHI broth (Brain Heart Infusion, DIFCO, Sparks, NV, USA). Five different microorganisms were used: four bacteria (*S. aureus*, *P. aeruginosa*, *E. coli*, and *E. faecalis*) and one fungus (*C. albicans*). The microorganisms were cultured under slow agitation, with bacteria at 37 °C and the fungus at 24 °C. The positive control for each test consisted of the growth of each individual microorganism alone. After 24 h, the growth of the microorganisms was assessed by measuring the OD600 nm of the growth medium using a D30 Biophotometer (Eppendorf, Hamburg, Germany).

### 2.6. Statistical Analysis

The antimicrobial activity experiment was performed in triplicate. Microorganisms' growth was quantified as the mean O.D 600 ± standard deviation (S.D.) and analysed using the non-parametric Dunnett test for multiple comparisons (SAS JMP Statistical Discovery

software v14 pro, Milan, Italy).  $p$  values of  $\leq 0.05$ ,  $\leq 0.01$ , and  $\leq 0.001$  were considered statistically significant, as indicated in the figure legends.

### 3. Results and Discussion

The coatings were initially deposited on Si(100) substrates to enable more accurate characterization by XRD and FTIR, excluding any interference from the Zn-Li alloy substrate. Additionally, non-substituted tricalcium phosphate ( $\beta$ -TCP) coatings were deposited alongside SrCu-TCP coatings for comparative analysis.

Figure 1 illustrates the XRD diffraction pattern of the TCP coating and its corresponding target material, as well as the SrCu-TCP coating and its corresponding target material. As evident from the diffraction patterns, both coatings exhibit an amorphous background, indicating their partial crystallinity.

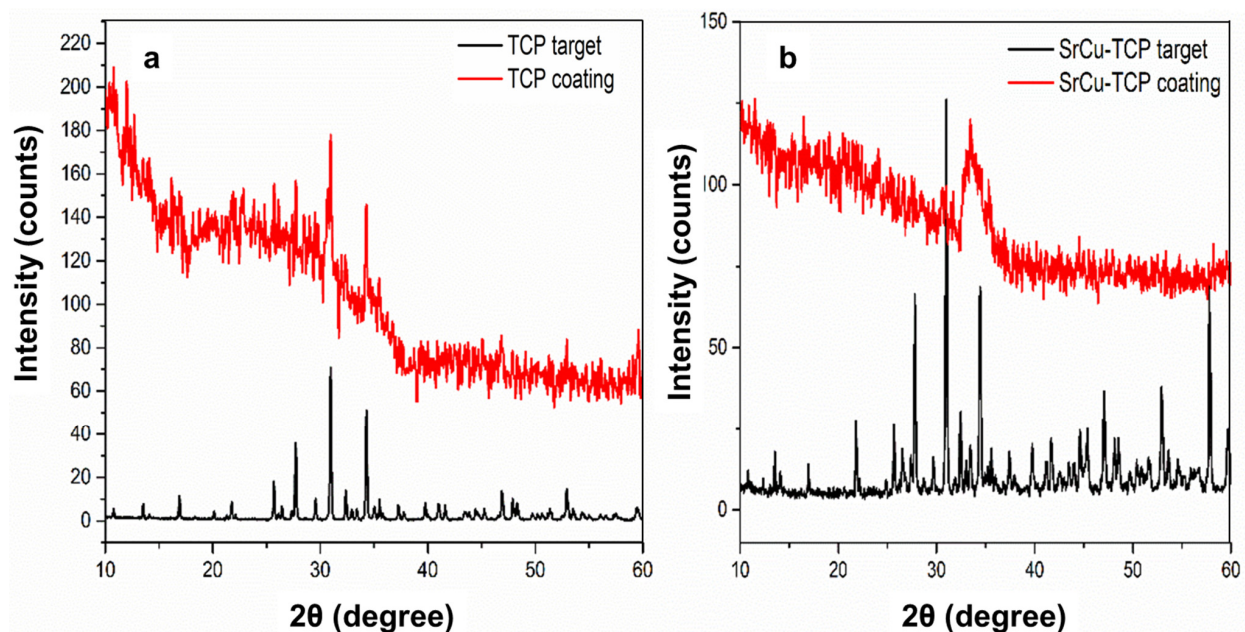


**Figure 1.** XRD patterns of (a) TCP coating deposited on Si substrate and corresponding target material, (b) SrCu-TCP coating deposited on Si substrate and corresponding target material.

Table 1 presents the  $2\theta$  position values of the most intense 21 peaks for both  $\beta$ -TCP and SrCu-TCP targets derived from their respective XRD patterns. The table also includes the shift position ( $\Delta 2\theta$ ) in degrees, calculated by subtracting the SrCu-TCP and  $\beta$ -TCP  $2\theta$  peak centre values. Additionally, the hkl Miller Index and the relative intensity (R.I.%) of each reflection are provided [64].

**Table 1.** The shifts for the main Bragg reflections of  $\beta$ -TCP and of double substituted SrCu-TCP.

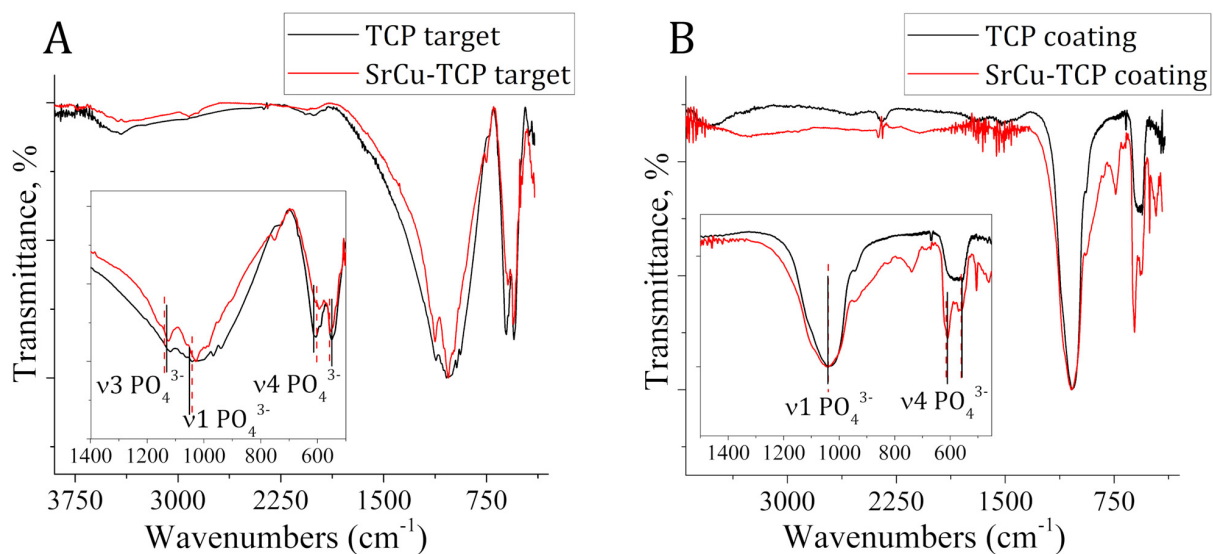
Peak Number	$\beta$ -TCP $2\theta$ Peak Position ( $^{\circ}$ )	SrCu-TCP $2\theta$ Peak Position ( $^{\circ}$ )	$\Delta 2\theta$	hkl Miller Index [64]	R.I.%
1	13.52	13.56	0.04	1 0 4	16
2	16.88	16.92	0.04	1 1 0	20
3	21.76	21.80	0.04	0 2 4	16
4	25.68	25.68	0.00	1 0 10	25
5	26.40	26.52	0.12	1 2 2	10
6	27.72	27.80	0.08	2 1 4	55
7	29.56	29.68	0.12	3 0 0	16
8	30.96	31.00	0.04	0 2 10	100
9	32.36	32.48	0.12	1 2 8	20
10	34.28	34.44	0.16	2 2 0	65

Table 1. Cont.

Peak Number	$\beta$ -TCP 2 $\theta$ Peak Position ( $^{\circ}$ )	SrCu-TCP 2 $\theta$ Peak Position ( $^{\circ}$ )	$\Delta 2\theta$	hkl Miller Index [64]	R.I.%
11	35.04	35.22	0.18	2 2 3	8
12	35.52	35.60	0.08	2 1 10	12
13	37.24	37.40	0.16	1 2 11	10
14	39.76	39.76	0.00	1 0 16	10
15	41.00	41.18	0.18	4 0 4	14
16	41.60	41.68	0.08	3 0 12	12
17	46.88	47.08	0.20	4 0 10	20
18	47.88	48.12	0.24	2 3 8	16
19	48.28	48.52	0.24	4 1 6	14
20	52.92	52.92	0.00	2 0 20	25
21	59.48	59.68	0.20	5 1 7	12

Observing the calculated shift position values ( $\Delta 2\theta$  column), it can be inferred that nearly all Bragg reflections of the SrCu-TCP target are shifted toward higher angles, with  $\Delta 2\theta$  values ranging from  $0^{\circ}$  to  $0.24^{\circ}$ . This suggests that the SrCu-TCP lattice generally exhibits shorter planar distances. Notably, lattice planes with Miller indexes  $h = 1$ ,  $k = 0$ , and  $l$  with relatively high values (10, 16) (peak numbers 4, 14, 20) remain unaffected by any angular shift, demonstrating a calculated  $\Delta 2\theta$  of  $0^{\circ}$ .

In Figure 2, the FTIR patterns collected from  $\beta$ -TCP and SrCu-TCP targets (A) and coatings (B), respectively, are presented. Within the main plot of each pattern, an inset showing the spectral window ranging from  $500$  to  $1500\text{ cm}^{-1}$  is presented, where the most prominent bands are highlighted.



**Figure 2.** FTIR spectra collected on TCP and SrCu-TCP compositions as targets (A) and coatings deposited on Si substrate (B). The  $500$ – $1500\text{ cm}^{-1}$  spectral window is highlighted. The centre position of the most significant bands is evidenced by a straight black line (TCP) and a dashed red line (SrCu-TCP).

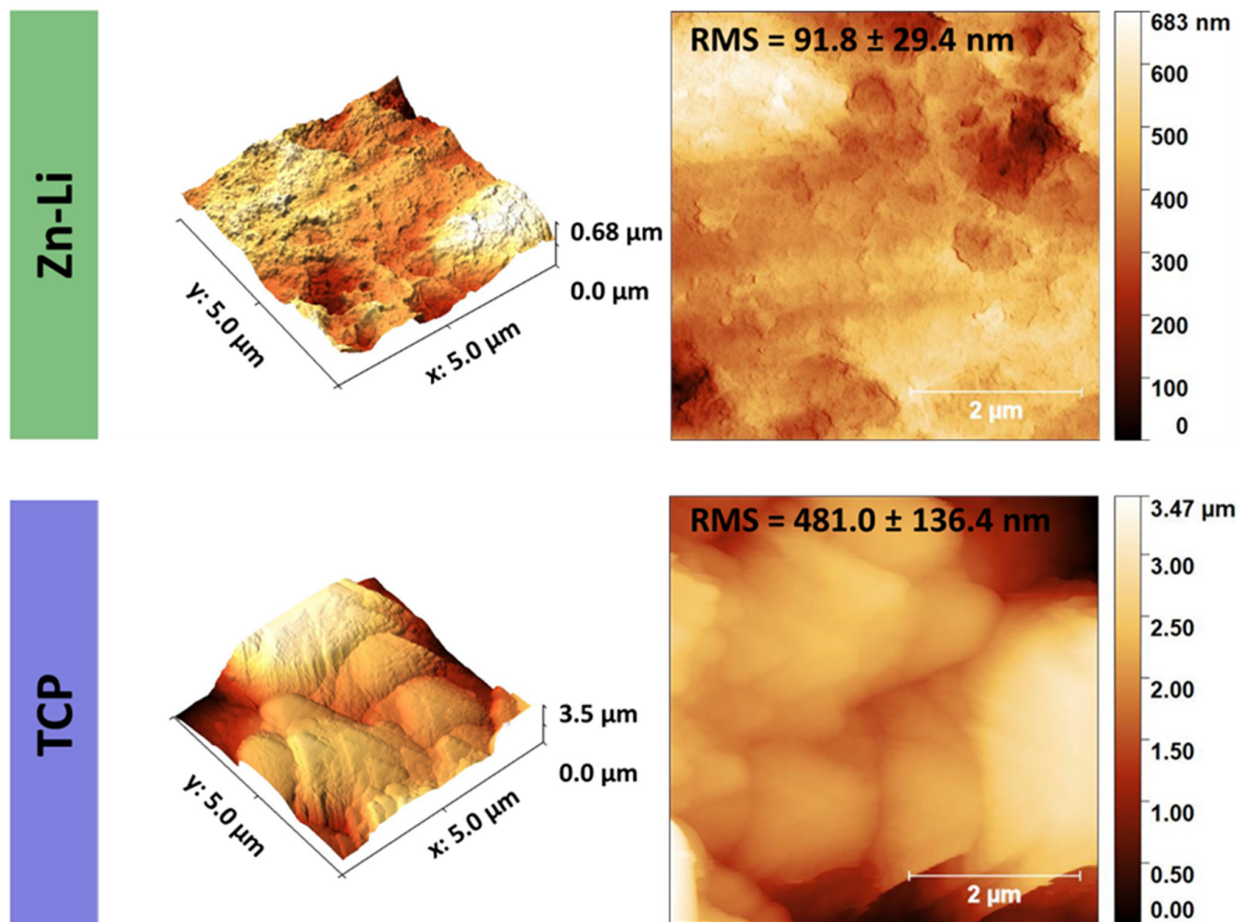
Figure 2A shows a general decreased degeneracy relative to the SrCu-TCP pattern compared to pure TCP. This difference is particularly evident for the IR absorption bands at  $945$ – $1087\text{ cm}^{-1}$ , attributable to the  $\nu 1$  and  $\nu 3$  modes of the  $\text{PO}_4^{3-}$  group, respectively [65,66]. Furthermore, the presence of Cu and Sr ions within the TCP matrix induced a shift in the position of all the observed main bands, as evidenced by the black straight line (TCP) and red dashed line (SrCu-TCP), allowing for the appreciation of the displacement in positions. The specific value for each band shift is reported in Table 2.

**Table 2.** FTIR band positions and band shifts for TCP and SrCu-TCP targets.

Mode	TCP Target ( $\text{cm}^{-1}$ )	SrCu-TCP Target ( $\text{cm}^{-1}$ )	Band Shift ( $\text{cm}^{-1}$ )
$\nu_3$	1120	1125	5
$\nu_1$	1042	1027	−15
$\nu_4$	605	590	15
$\nu_4$	549	554	−6

In Figure 2B, the patterns collected from TCP and SrCu-TCP coatings are reported and compared. It is possible to observe that the shape of the bands differs from those in the targets' IR spectra. In particular, both coatings' FTIR patterns exhibit narrower bands compared to those of the targets. Similar to what was observed for the targets, the presence of Sr and Cu in the TCP coating induced a variation in degeneracy, particularly evident for the bands at  $557\text{--}604\text{ cm}^{-1}$ , (the  $\nu_4$  mode of the  $\text{PO}_4^{3-}$  group) [66,67] where two sharp bands characterize the SrCu-TCP coating pattern. Finally, no significant shift was detectable from the comparison of pure TCP and SrCu-TCP coatings bands relative to the  $\nu_1$  mode of the  $\text{PO}_4^{3-}$ . For both compositions, the band is centred at around  $1038\text{ cm}^{-1}$ .

In Figure 3, typical 2D and 3D topographies of Zn-Li alloy, TCP coatings, and SrCu-TCP coatings on Zn-Li alloys are shown. Due to the deposition of particles of different sizes, it was observed that the surface of the Zn-Li sample is smoother than the others due to the absence of the coating. After coating, the average roughness of the TCP sample increases from  $91.8 \pm 29.4$  to  $481.0 \pm 136.4$  nm. Furthermore, it was found that the coating incorporated with Sr and Cu showed a further increase in roughness, reaching  $651.5 \pm 179.5$  nm.

**Figure 3.** Cont.

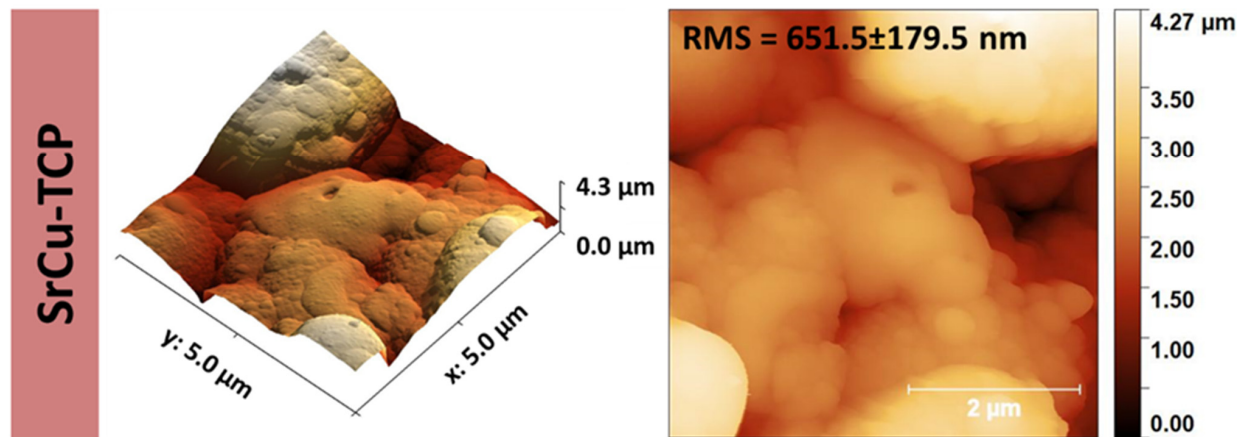


**Figure 3.** AFM 2D and 3D images of Zn-Li substrate and TCP and SrCu-TCP coatings on Zn-Li substrate.

The morphology of the SrCu-TCP coating on the Zn-Li substrate exhibits the typical characteristics observed in Pulsed Laser Deposited films, featuring droplets of varying sizes dispersed within a compact matrix. SEM images in Figure 4 demonstrate the compact globular morphology of the deposited SrCu-TCP coatings.

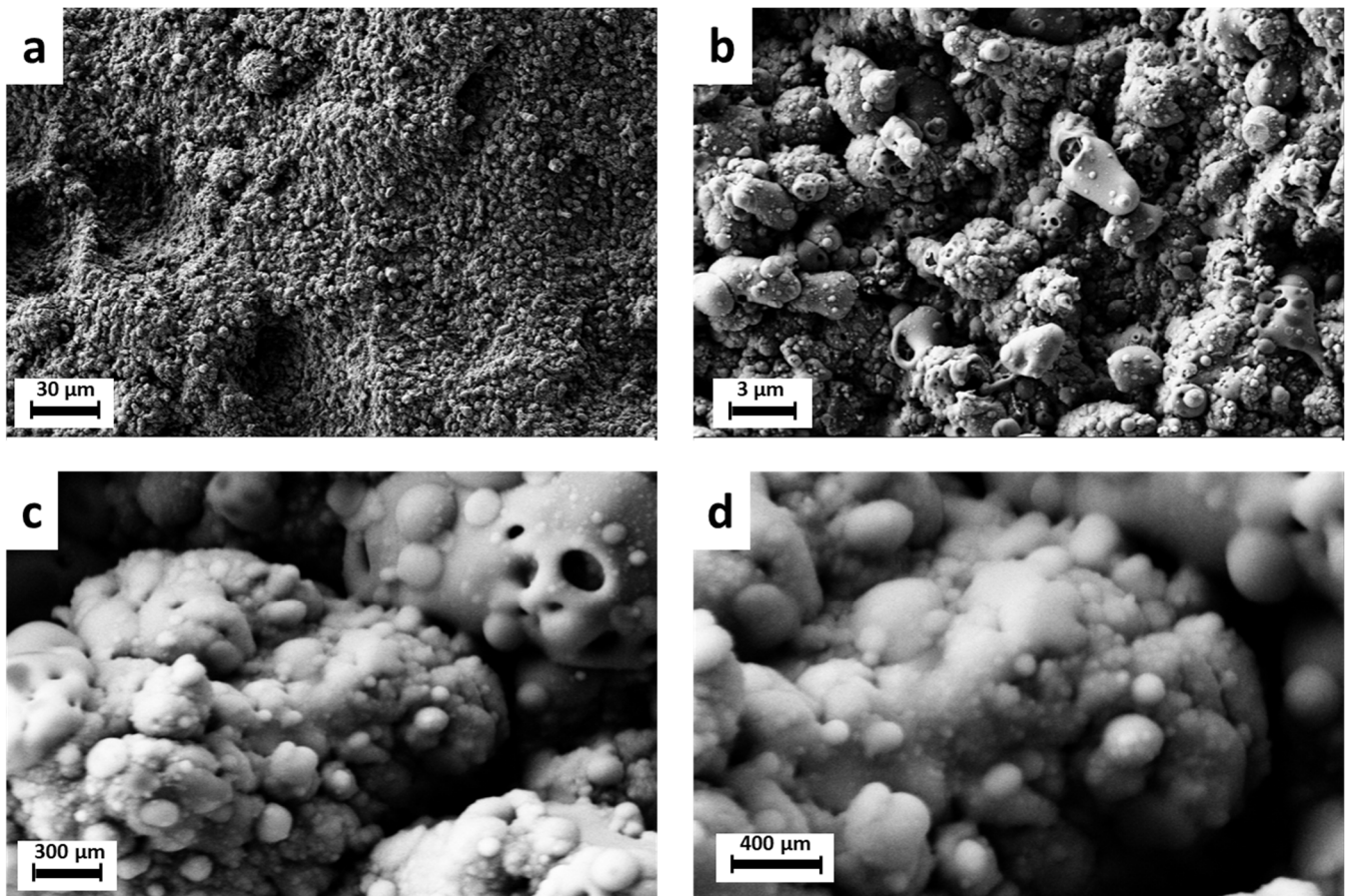


**Figure 4.** SEM images of SrCu-TCP coating on Zn-Li substrate at 1 kx (a), 10 kx (b), 50 kx (c), and 100 kx (d) magnifications.



To assess the thickness of the deposited coatings, cross-section SEM images were acquired. As depicted in the SEM images shown in Figure 5, the coatings exhibit a thickness within the range of a few micrometres, specifically 3–3.5  $\mu\text{m}$ .

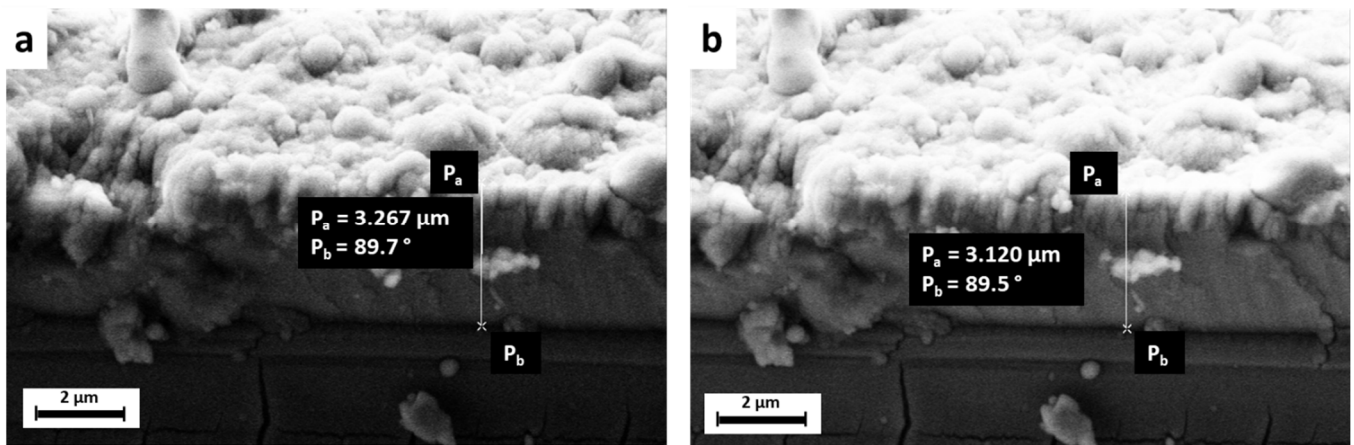


Figure 5. SEM cross section images of SrCu-TCP coating on Zn-Li substrate. (a) Area 1 and (b) Area 2.

SEM-EDX measurements were conducted to analyse the composition of the coatings, with the results presented in Figure 6 and Table 3. The data indicate that the coatings contain approximately  $4.10 \pm 0.18$  wt% of Cu and  $6.54 \pm 0.33$  wt% of Sr. Additionally, a minor amount of Zn is detected, originating from the Zn-Li substrate.

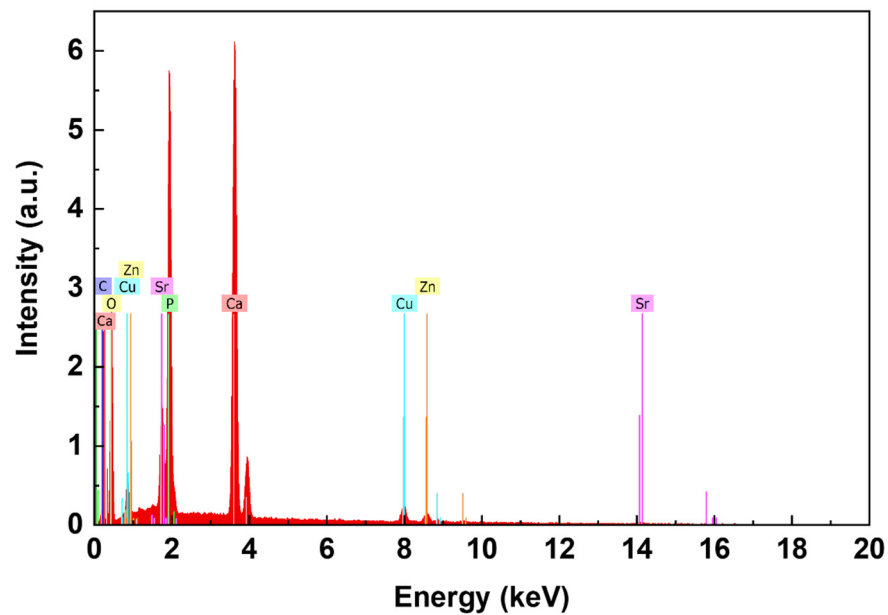


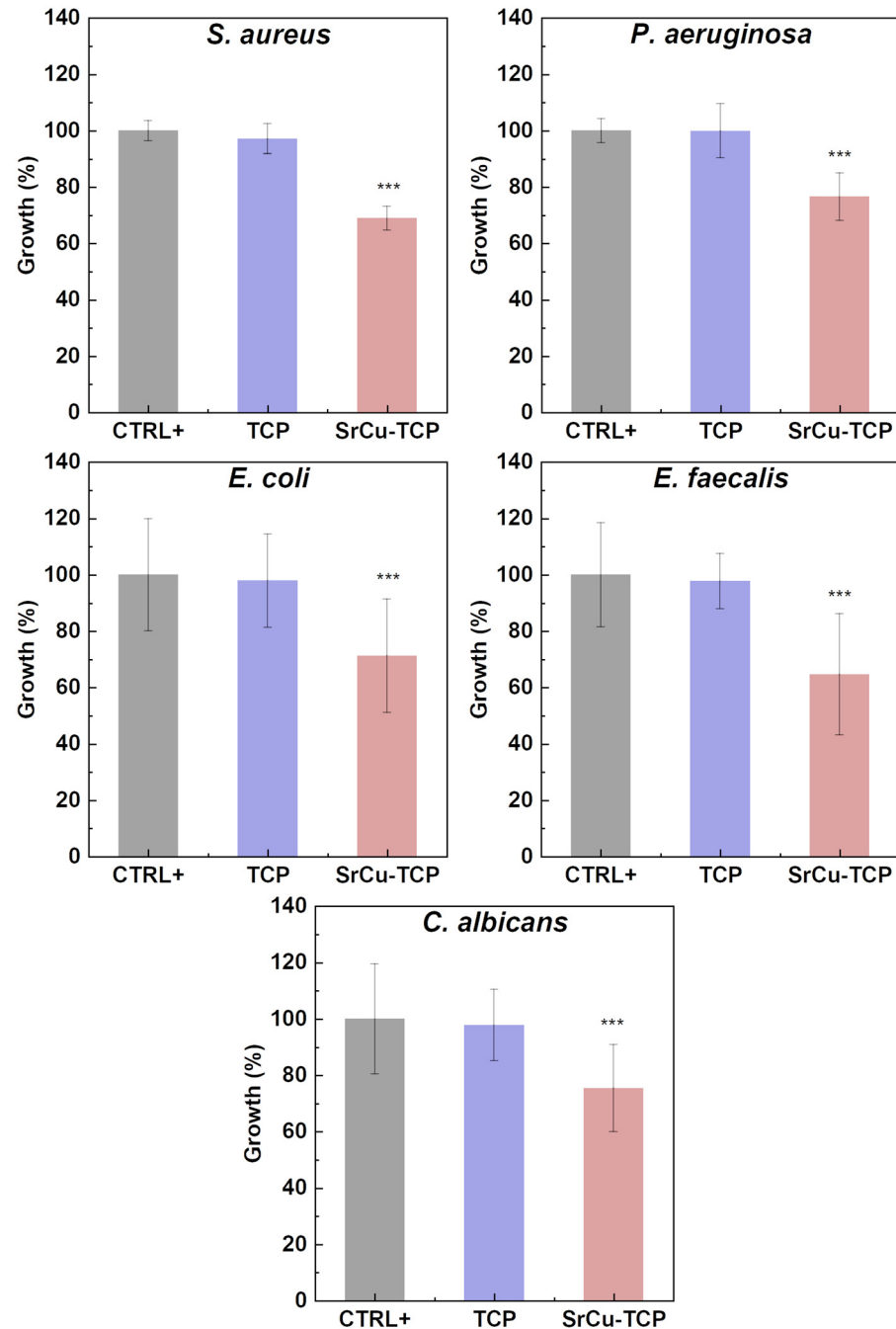
Figure 6. SEM-EDX spectrum of SrCu-TCP coating on Zn-Li substrate.

Table 3. Sr and Cu content in targets and deposited SrCu-TCP coatings.

EDX (Coatings)	Sr, wt%			Cu, wt%		
	AAS (Targets)	Theoretical Value, in $\text{Ca}_{2.5}\text{Sr}_{0.25}\text{Cu}_{0.25}(\text{PO}_4)_2$ Powder	EDX (Coatings)	AAS (Targets)	Theoretical Value, in $\text{Ca}_{2.5}\text{Sr}_{0.25}\text{Cu}_{0.25}(\text{PO}_4)_2$ Powder	
$6.54 \pm 0.33$	$6.68 \pm 0.05$	6.71	$4.10 \pm 0.18$	$4.78 \pm 0.05$	4.84	

The results related to the growth of microorganisms (*S. aureus*, *P. aeruginosa*, *E. coli*, *E. faecalis*, and *C. albicans*) in the presence and absence of SrCu-TCP coatings on Zn-Li

alloys are reported in Table 4 and illustrated in Figure 7. The data provided in the table include the mean OD600 values, standard deviations (SD), percentage of growth, and percentage of growth inhibition derived from three independent experiments. The growth of each organism was assessed after 24 h of incubation at their respective optimal growth temperatures. The microorganisms cultured alone (without the coated substrates) served as the positive control of the experiment (CTR+).



**Figure 7.** Growth rate of *S. aureus*, *P. aeruginosa*, *E. coli*, and *E. faecalis* bacteria strains and *C. albicans* fungus grown in the presence of control sample and TCP and SrCu-TPC coatings on Zn-Li alloy substrate. The growth percentage is calculated on the OD600 resulting from three independent experiments and presented as mean values  $\pm$  standard deviation (SD), compared to the values of the positive control corresponding to 100%.  $p$  values (Dunnnett test):  $p < 0.001$  \*\*\* compared to positive control.

**Table 4.** Growth rate of bacteria (*S. aureus*, *P. aeruginosa*, *E. coli* and *E. faecalis*) and a fungus (*C. albicans*) grown in the presence of control sample, TCP, and SrCu-TPC coatings on Zn-Li alloy substrate. The growth percentage was calculated on the OD600 resulting from three independent experiments and presented as mean values  $\pm$  standard deviation (SD).

	OD 600 nm	SD	% Growth	% Inhibition
<i>S. aureus</i>				
CTR+	1.009	0.03	100.0	0.0
TCP	0.980	0.05	97.1	2.9
SrCu-TCP	0.695	0.04	68.9	31.1
<i>P. aeruginosa</i>				
CTR+	0.984	0.03	100.0	0.0
TCP	0.983	0.09	99.9	0.1
SrCu-TCP	0.753	0.08	76.5	23.5
<i>E. coli</i>				
CTR+	1.204	0.17	100.0	0.0
TCP	1.179	0.11	97.9	2.1
SrCu-TCP	0.858	0.21	71.3	28.7
<i>E. faecalis</i>				
CTR+	0.995	0.17	100.0	0.0
TCP	0.973	0.07	97.8	2.2
SrCu-TCP	0.643	0.21	64.7	35.3
<i>C. albicans</i>				
CTR+	0.810	0.15	100.0	0.0
TCP	0.792	0.09	97.8	2.2
SrCu-TCP	0.611	0.12	75.4	24.6

The growth of all microorganisms on TCP is statistically comparable to the growth of the positive control (without samples). Statistically significant growth inhibition was observed in all tested microorganisms when grown in the presence of SrCu-TPC. In particular, the inhibition of the growth of microorganisms is 31.1% for *S. aureus*, 23.5% for *P. aeruginosa*, 28.7% for *E. coli*, 35.3% for *E. faecalis*, and 24.6% for *C. albicans*.

In contrast, our previous study [57], focused on double-substituted tricalcium phosphate powder—SrCu-TCP, revealed notably higher growth inhibition rates. The SrCu-TCP powder exhibited a remarkable inhibition of growth, reaching 92.0%, 95.5%, 64.9%, 96.3%, and 70.9% against *S. aureus*, *P. aeruginosa*, *E. coli*, *E. faecalis*, and *C. albicans*, respectively. Such a considerable difference could potentially be attributed to the reduced amount of material present in the coating.

In our previous study [44], focusing on double-substituted tricalcium phosphate coatings applied to the same Zn-Li alloys but containing Strontium and Manganese substitution—SrMn-TCP, the inhibition of 12.2% of *S. aureus*, 9.4% of *P. aeruginosa*, and 9.0% of *E. coli*, 9.7% of *E. faecalis* was registered. The SrMn-TCP-coated Zn-Li alloys were effective in inhibiting the growth of fungus *C. albicans*, achieving approximately a 50% inhibition rate.

Also in this case, for SrMn-TCP powder [57], a higher inhibition growth was registered compared to the coatings. Indeed, SrMn-TCP powder demonstrated a substantial inhibition of growth, with rates of 57.8% for *S. aureus*, 92.9% for *P. aeruginosa*, 19% for *E. coli*, 67.4% for *E. faecalis*, and 41.9% for *C. albicans*.

Table 5 below summarizes the results on microorganisms' inhibition obtained in the present study and reported in the cited above literature.

**Table 5.** Summary of the results on microbial inhibition obtained in the present study and reported in the literature.

Sample	% Inhibition					Reference
	<i>S. aureus</i>	<i>P. aeruginosa</i>	<i>E. coli</i>	<i>E. faecalis</i>	<i>C. albicans</i>	
SrCu-TCP (coating)	31.1	23.5	28.7	35.3	24.6	present study
SrCu-TCP (powder)	92.0	95.5	64.9	96.3	70.9	[57]
SrMn-TCP (coating)	12.2	9.4	9.0	9.7	50.0	[44]
SrMn-TCP (powder)	57.8	92.9	19.0	67.4	41.9	[57]

#### 4. Conclusions

Partially-crystalline SrCu-TCP coatings were deposited by Pulsed Laser Deposition technique onto the Zn-Li alloy substrates. The composition analysis revealed approximately 6.5 wt% Sr and 4.1 wt% Cu within the coatings. The incorporation of Sr and Cu into the crystal lattice was evidenced by observed shifts in diffraction peaks and IR bands.

Morphological examination exhibited compact micro-globular structures in the coatings. The average surface roughness of the TCP coating was measured at  $481.0 \pm 136.4$  nm, while the SrCu-TCP coating exhibited a further increase, reaching  $651.5 \pm 179.5$  nm. The thickness of the coatings, determined by SEM, ranged between 3–3.5  $\mu$ m.

Our study showed statistically significant inhibition of the growth in all tested microorganisms in the presence of SrCu-TCP coatings, while microorganisms cultured solely on TCP coatings did not exhibit significant growth inhibition.

The SrCu-TCP surface demonstrated good antimicrobial efficacy, achieving inhibition of the growth ranging between 23.5% and 35.3%. Specifically, for *S. aureus*, the inhibition was at 31.1%, for *P. aeruginosa* at 23.5%, for *E. coli* at 28.7%, for *E. faecalis* at 35.3%, and for *C. albicans* at 24.6%. These results highlight the antimicrobial characteristics of the SrCu-TCP surface on Zn-Li alloy, making it a promising candidate for applications requiring inhibition of both bacterial and fungal growth.

**Author Contributions:** Conceptualization, J.V.R. and Y.Z.; methodology, J.V.R., A.D.B., K.B., M.F., I.V.F., G.C.C., R.T., T.K.S. and Y.Z.; validation, A.D.B., K.B., M.F., I.V.F., G.C.C., R.T. and T.K.S.; formal analysis, M.C., K.B., M.F., G.C.C. and T.K.S.; investigation, A.D.B., M.C., K.B., M.F. and I.V.F.; resources, J.V.R., A.D.B., K.B., I.V.F. and R.T.; data curation, A.D.B., M.C., K.B., M.F., G.C.C. and T.K.S.; writing—original draft preparation, J.V.R.; writing—review and editing, J.V.R. and G.C.C.; visualization, J.V.R. and G.C.C.; supervision, J.V.R.; project administration, J.V.R.; funding acquisition, J.V.R., K.B. and Y.Z. All authors have read and agreed to the published version of the manuscript.

**Funding:** J.V.R. and Y.Z. thank the bilateral project CNR (Italy)—NSFC (China) 2021–2022 and the International Cooperation and Exchange program of NSFC-CNR (Grant No. 52011530392). Financial support of the Italian Ministry of Health, grants IZSLT 10/22 RC and IZSLT 01/23 RC is gratefully acknowledged.

**Institutional Review Board Statement:** Not applicable.

**Informed Consent Statement:** Not applicable.

**Data Availability Statement:** The experimental data are available upon a reasonable and official request to the corresponding author.

**Acknowledgments:** Technical assistance of Marco Ortenzi, Massimo Di Menno Di Bucchianico and Luca Imperatori is gratefully acknowledged.

**Conflicts of Interest:** The authors declare no conflicts of interest.

#### References

- Shi, Z.-Z.; Gao, X.-X.; Zhang, H.-J.; Liu, X.-F.; Li, H.-Y.; Zhou, C.; Yin, Y.-X.; Wang, L.-N. Design biodegradable Zn alloys: Second phases and their significant influences on alloy properties. *Bioact. Mater.* **2020**, *5*, 210–218. [[CrossRef](#)] [[PubMed](#)]
- Young, J.; Reddy, R.G. Synthesis, mechanical properties, and in vitro corrosion behavior of biodegradable Zn–Li–Cu alloys. *J. Alloys Compd.* **2020**, *844*, 156257. [[CrossRef](#)]

3. Zhao, S.; Seitz, J.-M.; Eifler, R.; Maier, H.J.; Guillory, R.J.; Earley, E.J.; Drelich, A.; Goldman, J.; Drelich, J.W. Zn-Li alloy after extrusion and drawing: Structural, mechanical characterization, and biodegradation in abdominal aorta of rat. *Mater. Sci. Eng. C* **2017**, *76*, 301–312. [[CrossRef](#)]
4. Li, H.; Huang, Y.; Ji, X.; Wen, C.; Wang, L.-N. Fatigue and corrosion fatigue behaviors of biodegradable Zn-Li and Zn-Cu-Li under physiological conditions. *J. Mater. Sci. Technol.* **2022**, *131*, 48–59. [[CrossRef](#)]
5. Chen, Y.; Xu, Z.; Smith, C.; Sankar, J. Recent advances on the development of magnesium alloys for biodegradable implants. *Acta Biomater.* **2014**, *10*, 4561–4573. [[CrossRef](#)]
6. Staiger, M.P.; Pietak, A.M.; Huadmai, J.; Dias, G. Magnesium and its alloys as orthopedic biomaterials: A review. *Biomaterials* **2006**, *27*, 1728–1734. [[CrossRef](#)]
7. Farè, S.; Ge, Q.; Vedani, M.; Vimercati, G.; Gastaldi, D.; Migliavacca, F.; Petrini, L.; Trasatti, S. Evaluation of material properties and design requirements for biodegradable magnesium stents. *Matéria* **2010**, *15*, 96–103. [[CrossRef](#)]
8. Li, H.; Wen, J.; Liu, Y.; He, J.; Shi, H.; Tian, P. Progress in Research on Biodegradable Magnesium Alloys: A Review. *Adv. Eng. Mater.* **2020**, *22*, 2000213. [[CrossRef](#)]
9. Costantino, M.D.; Schuster, A.; Helmholz, H.; Meyer-Rachner, A.; Willumeit-Römer, R.; Luthringer-Feyerabend, B.J.C. Inflammatory response to magnesium-based biodegradable implant materials. *Acta Biomater.* **2020**, *101*, 598–608. [[CrossRef](#)]
10. Li, M.; Ren, L.; Li, L.; He, P.; Lan, G.; Zhang, Y.; Yang, K. Cytotoxic Effect on Osteosarcoma MG-63 Cells by Degradation of Magnesium. *J. Mater. Sci. Technol.* **2014**, *30*, 888–893. [[CrossRef](#)]
11. Henderson, S.E.; Verdelis, K.; Maiti, S.; Pal, S.; Chung, W.L.; Chou, D.-T.; Kumta, P.N.; Almarza, A.J. Magnesium alloys as a biomaterial for degradable craniofacial screws. *Acta Biomater.* **2014**, *10*, 2323–2332. [[CrossRef](#)]
12. Song, G. Control of biodegradation of biocompatible magnesium alloys. *Corros. Sci.* **2007**, *49*, 1696–1701. [[CrossRef](#)]
13. Zhang, Z.; Jia, Q.; Wu, X.; Cao, X.; Xu, C.; Zhang, J.; Yang, W. Study on microstructure and dynamic corrosion behavior of degradable Mg–Y–Zn–Zr alloy with different Sr contents. *Mater. Res. Express* **2019**, *6*, 125418. [[CrossRef](#)]
14. Sanchez, A.H.M.; Luthringer, B.J.C.; Feyerabend, F.; Willumeit, R. Mg and Mg alloys: How comparable are in vitro and in vivo corrosion rates? A review. *Acta Biomater.* **2015**, *13*, 16–31. [[CrossRef](#)] [[PubMed](#)]
15. Nguyen, T.; Waterman, J.; Staiger, M.; Woodfield, T. Controlling in vitro corrosion rate of pure Mg with rough surface texture via biomimetic coating systems. *Corros. Eng. Sci. Technol.* **2012**, *47*, 358–364. [[CrossRef](#)]
16. Tian, Y.; Shao, Y.; Yu, Q.; Guo, S.; Dang, R.; Du, Y.; Zhu, G.; Lyu, S.; Chen, M. Investigating the corrosion behavior of as-cast Mg–Zn–Ca alloys with the same Zn/Ca atomic ratio by in situ observation. *Mater. Corros.* **2024**. [[CrossRef](#)]
17. Hara, T.; Takeda, T.-A.; Takagishi, T.; Fukue, K.; Kambe, T.; Fukada, T. Physiological roles of zinc transporters: Molecular and genetic importance in zinc homeostasis. *J. Physiol. Sci.* **2017**, *67*, 283–301. [[CrossRef](#)]
18. Lowe, N.M.; Fraser, W.D.; Jackson, M.J. Is there a potential therapeutic value of copper and zinc for osteoporosis? *Proc. Nutr. Soc.* **2009**, *61*, 181–185. [[CrossRef](#)] [[PubMed](#)]
19. Komarova, E.G.; Sharkeev, Y.P.; Sedelnikova, M.B.; Prosolov, K.A.; Khlusov, I.A.; Prymak, O.; Epple, M. Zn- or Cu-Containing CaP-Based Coatings Formed by Micro-arc Oxidation on Titanium and Ti-40Nb Alloy: Part I—Microstructure, Composition and Properties. *Materials* **2020**, *13*, 4116. [[CrossRef](#)]
20. Hernández-Escobar, D.; Champagne, S.; Yilmazer, H.; Dikici, B.; Boehlert, C.J.; Hermawan, H. Current status and perspectives of zinc-based absorbable alloys for biomedical applications. *Acta Biomater.* **2019**, *97*, 1–22. [[CrossRef](#)]
21. O'Connor, J.P.; Kanjilal, D.; Teitelbaum, M.; Lin, S.S.; Cottrell, J.A. Zinc as a Therapeutic Agent in Bone Regeneration. *Materials* **2020**, *13*, 2211. [[CrossRef](#)]
22. Molenda, M.; Kolmas, J. The Role of Zinc in Bone Tissue Health and Regeneration—A Review. *Biol. Trace Elem. Res.* **2023**, *201*, 5640–5651. [[CrossRef](#)]
23. Cerovic, A.; Miletic, I.; Sobajic, S.; Blagojevic, D.; Radusinovic, M.; El-Sohemy, A. Effects of zinc on the mineralization of bone nodules from human osteoblast-like cells. *Biol. Trace Elem. Res.* **2007**, *116*, 61–71. [[CrossRef](#)]
24. Hadley, K.B.; Newman, S.M.; Hunt, J.R. Dietary zinc reduces osteoclast resorption activities and increases markers of osteoblast differentiation, matrix maturation, and mineralization in the long bones of growing rats. *J. Nutr. Biochem.* **2010**, *21*, 297–303. [[CrossRef](#)] [[PubMed](#)]
25. Seo, H.-J.; Cho, Y.-E.; Kim, T.; Shin, H.-I.; Kwun, I.-S. Zinc may increase bone formation through stimulating cell proliferation, alkaline phosphatase activity and collagen synthesis in osteoblastic MC3T3-E1 cells. *Nutr. Res. Pr.* **2010**, *4*, 356–361. [[CrossRef](#)] [[PubMed](#)]
26. Moonga, B.S.; Dempster, D.W. Zinc is a potent inhibitor of osteoclastic bone resorption in vitro. *J. Bone Miner. Res.* **1995**, *10*, 453–457. [[CrossRef](#)] [[PubMed](#)]
27. Ma, J.; Zhao, N.; Zhu, D. Endothelial Cellular Responses to Biodegradable Metal Zinc. *ACS Biomater. Sci. Eng.* **2015**, *1*, 1174–1182. [[CrossRef](#)]
28. Fosca, M.; Streza, A.; Antoniac, I.V.; Vadalà, G.; Rau, J.V. Ion-Doped Calcium Phosphate-Based Coatings with Antibacterial Properties. *J. Funct. Biomater.* **2023**, *14*, 250. [[CrossRef](#)]
29. Maleki-Ghaleh, H.; Siadati, M.H.; Fallah, A.; Koc, B.; Kavanlouei, M.; Khademi-Azandehi, P.; Moradpur-Tari, E.; Omidi, Y.; Barar, J.; Beygi-Khosrowshahi, Y.; et al. Antibacterial and Cellular Behaviors of Novel Zinc-Doped Hydroxyapatite/Graphene Nanocomposite for Bone Tissue Engineering. *Int. J. Mol. Sci.* **2021**, *22*, 9564. [[CrossRef](#)]

30. Laskus-Zakrzewska, A.; Zgadaj, A.; Kolmas, J. Synthesis and physicochemical characterization of Zn-doped brushite. *Ceram. Int.* **2021**, *47*, 7798–7804. [[CrossRef](#)]
31. Cruz, R.; Calasans-Maia, J.; Sartoretto, S.; Moraschini, V.; Rossi, A.M.; Louro, R.S.; Granjeiro, J.M.; Calasans-Maia, M.D. Does the incorporation of zinc into calcium phosphate improve bone repair? A systematic review. *Ceram. Int.* **2018**, *44*, 1240–1249. [[CrossRef](#)]
32. Li, Z.; Shi, Z.-Z.; Hao, Y.; Li, H.-F.; Zhang, H.-J.; Liu, X.-F.; Wang, L.-N. Insight into role and mechanism of Li on the key aspects of biodegradable ZnLi alloys: Microstructure evolution, mechanical properties, corrosion behavior and cytotoxicity. *Mater. Sci. Eng. C* **2020**, *114*, 111049. [[CrossRef](#)] [[PubMed](#)]
33. Gong, H.; Wang, K.; Strich, R.; Zhou, J.G. In vitro biodegradation behavior, mechanical properties, and cytotoxicity of biodegradable Zn–Mg alloy. *J. Biomed. Mater. Res. Part B Appl. Biomater.* **2015**, *103*, 1632–1640. [[CrossRef](#)] [[PubMed](#)]
34. Wang, M.; Yang, L.; Zhu, X.; Yang, L.; Shen, J.; Lu, T.; Liu, H.; Song, Z. Corrosion Mechanisms of a Biodegradable Zn-0.4Li Alloy in Simulated Gastrointestinal Environment. *Coatings* **2023**, *13*, 529. [[CrossRef](#)]
35. Young, W. Review of Lithium Effects on Brain and Blood. *Cell Transplant.* **2009**, *18*, 951–975. [[CrossRef](#)] [[PubMed](#)]
36. Aral, H.; Vecchio-Sadus, A. Toxicity of lithium to humans and the environment—A literature review. *Ecotoxicol. Environ. Saf.* **2008**, *70*, 349–356. [[CrossRef](#)]
37. Tong, X.; Shen, T.; Zhou, X.; Zeng, J.; Tao, J.; Munir, K.; Li, Y.; Huang, S.; Wu, X.; Ma, J.; et al. Biodegradable Zn–Cu–Li alloys with ultrahigh strength, ductility, antibacterial ability, cytocompatibility, and suitable degradation rate for potential bone-implant applications. *Smart Mater. Manuf.* **2023**, *1*, 100012. [[CrossRef](#)]
38. Zhang, Y.; Lu, Y.; Xu, X.; Chen, L.; Xiao, T.; Luo, X.; Yan, Y.; Li, D.; Dai, Y.; Yu, K. Microstructure, Corrosion Behaviors in Different Simulated Body Fluids and Cytotoxicity of Zn–Li Alloy as Biodegradable Material. *Mater. Trans.* **2019**, *60*, 583–586. [[CrossRef](#)]
39. Clément-Lacroix, P.; Ai, M.; Morvan, F.; Roman-Roman, S.; Vayssière, B.; Belleville, C.; Estrera, K.; Warman, M.L.; Baron, R.; Rawadi, G. Lrp5-independent activation of Wnt signaling by lithium chloride increases bone formation and bone mass in mice. *Proc. Natl. Acad. Sci. USA* **2005**, *102*, 17406–17411. [[CrossRef](#)]
40. Zamani, A.; Omrani, G.R.; Nasab, M.M. Lithium's effect on bone mineral density. *Bone* **2009**, *44*, 331–334. [[CrossRef](#)]
41. Salahshoor, M.; Guo, Y. Biodegradable Orthopedic Magnesium-Calcium (MgCa) Alloys, Processing, and Corrosion Performance. *Materials* **2012**, *5*, 135–155. [[CrossRef](#)] [[PubMed](#)]
42. Zhang, C.; Zeng, R.; Liu, C.; Gao, J. Comparison of calcium phosphate coatings on Mg–Al and Mg–Ca alloys and their corrosion behavior in Hank's solution. *Surf. Coat. Technol.* **2010**, *204*, 3636–3640. [[CrossRef](#)]
43. Dorozhkin, S.V. Calcium orthophosphate coatings on magnesium and its biodegradable alloys. *Acta Biomater.* **2014**, *10*, 2919–2934. [[CrossRef](#)] [[PubMed](#)]
44. Rau, J.V.; De Bonis, A.; Teghil, R.; Curcio, M.; Fadeeva, I.V.; Barbaro, K.; Di Menno Di Bucchianico, M.; Fosca, M.; Zheng, Y. Double Substituted with Manganese and Strontium Tricalcium Phosphate Coatings on Zinc-Lithium Biodegradable Alloys for Biomedical Implant Applications. *Coatings* **2023**, *13*, 36. [[CrossRef](#)]
45. Li, H.F.; Shi, Z.Z.; Wang, L.N. Opportunities and challenges of biodegradable Zn-based alloys. *J. Mater. Sci. Technol.* **2020**, *46*, 136–138. [[CrossRef](#)]
46. Xing, H.; Tang, Y.; Fa, X.; Zhang, H.; Shi, Z.; Yao, S.; Wang, L. Enhanced Biocompatibility and Osteogenic Property of Biodegradable Zn-0.5Li Alloy through Calcium–Phosphorus Coating. *Coatings* **2024**, *14*, 350. [[CrossRef](#)]
47. Bohner, M.; Santoni, B.L.G.; Döbelin, N.  $\beta$ -tricalcium phosphate for bone substitution: Synthesis and properties. *Acta Biomater.* **2020**, *113*, 23–41. [[CrossRef](#)]
48. Fadeeva, I.V.; Deyneko, D.V.; Forysenkova, A.A.; Morozov, V.A.; Akhmedova, S.A.; Kirsanova, V.A.; Sviridova, I.K.; Sergeeva, N.S.; Rodionov, S.A.; Udyanskaya, I.L.; et al. Strontium Substituted  $\beta$ -Tricalcium Phosphate Ceramics: Physicochemical Properties and Cytocompatibility. *Molecules* **2022**, *27*, 6085. [[CrossRef](#)]
49. Fadeeva, I.V.; Lazoryak, B.I.; Davidova, G.A.; Murzakhanov, F.F.; Gabbasov, B.F.; Petrakova, N.V.; Fosca, M.; Barinov, S.M.; Vadalà, G.; Uskoković, V.; et al. Antibacterial and cell-friendly copper-substituted tricalcium phosphate ceramics for biomedical implant applications. *Mater. Sci. Eng. C* **2021**, *129*, 112410. [[CrossRef](#)]
50. Kazakova, G.; Safronova, T.; Golubchikov, D.; Shevtsova, O.; Rau, J.V. Resorbable Mg<sup>2+</sup>-Containing Phosphates for Bone Tissue Repair. *Materials* **2021**, *14*, 4857. [[CrossRef](#)]
51. Rau, J.V.; Fadeeva, I.V.; Fomin, A.S.; Barbaro, K.; Galvano, E.; Ryzhov, A.P.; Murzakhanov, F.; Gafurov, M.; Orlinskii, S.; Antoniac, I.; et al. Sic Parvis Magna: Manganese-Substituted Tricalcium Phosphate and Its Biophysical Properties. *ACS Biomater. Sci. Eng.* **2019**, *5*, 6632–6644. [[CrossRef](#)]
52. Fadeeva, I.V.; Kalita, V.I.; Komlev, D.I.; Radiuk, A.A.; Fomin, A.S.; Davidova, G.A.; Fursova, N.K.; Murzakhanov, F.F.; Gafurov, M.R.; Fosca, M.; et al. In Vitro Properties of Manganese-Substituted Tricalcium Phosphate Coatings for Titanium Biomedical Implants Deposited by Arc Plasma. *Materials* **2020**, *13*, 4411. [[CrossRef](#)] [[PubMed](#)]
53. Antoniac, I.V.; Filipescu, M.; Barbaro, K.; Bonciu, A.; Birjega, R.; Cotrut, C.M.; Galvano, E.; Fosca, M.; Fadeeva, I.V.; Vadalà, G.; et al. Iron Ion-Doped Tricalcium Phosphate Coatings Improve the Properties of Biodegradable Magnesium Alloys for Biomedical Implant Application. *Adv. Mater. Interfaces* **2020**, *7*, 2000531. [[CrossRef](#)]
54. Fadeeva, I.V.; Goldberg, M.A.; Preobrazhensky, I.I.; Mamin, G.V.; Davidova, G.A.; Agafonova, N.V.; Fosca, M.; Russo, F.; Barinov, S.M.; Cavalu, S.; et al. Improved cytocompatibility and antibacterial properties of zinc-substituted brushite bone cement based on  $\beta$ -tricalcium phosphate. *J. Mater. Sci. Mater. Med.* **2021**, *32*, 99. [[CrossRef](#)] [[PubMed](#)]

55. Božić Cvijan, B.; Korać Jačić, J.; Bajčetić, M. The Impact of Copper Ions on the Activity of Antibiotic Drugs. *Molecules* **2023**, *28*, 5133. [CrossRef] [PubMed]
56. Salah, I.; Parkin, I.P.; Allan, E. Copper as an antimicrobial agent: Recent advances. *RSC Adv.* **2021**, *11*, 18179–18186. [CrossRef]
57. Deyneko, D.V.; Fadeeva, I.V.; Borovikova, E.Y.; Dzhevakov, P.B.; Slukin, P.V.; Zheng, Y.; Xia, D.; Lazoryak, B.I.; Rau, J.V. Antimicrobial properties of co-doped tricalcium phosphates  $\text{Ca}_{3-2x}(\text{M}'\text{M}'')_x(\text{PO}_4)_2$  ( $\text{M} = \text{Zn}^{2+}, \text{Cu}^{2+}, \text{Mn}^{2+}$  and  $\text{Sr}^{2+}$ ). *Ceram. Int.* **2022**, *48*, 29770–29781. [CrossRef]
58. Ribeiro, M.; Monteiro, F.J.; Ferraz, M.P. Infection of orthopedic implants with emphasis on bacterial adhesion process and techniques used in studying bacterial-material interactions. *Biomatter* **2012**, *2*, 176–194. [CrossRef]
59. Wang, M.; Tang, T. Surface treatment strategies to combat implant-related infection from the beginning. *J. Orthop. Transl.* **2019**, *17*, 42–54. [CrossRef]
60. Aggarwal, V.K.; Bakhshi, H.; Ecker, N.U.; Parvizi, J.; Gehrke, T.; Kendoff, D. Organism Profile in Periprosthetic Joint Infection: Pathogens Differ at Two Arthroplasty Infection Referral Centers in Europe and in the United States. *J. Knee Surg.* **2014**, *27*, 399–406. [CrossRef]
61. Miquel, S.; Lagrèfeuille, R.; Souweine, B.; Forestier, C. Anti-biofilm Activity as a Health Issue. *Front. Microbiol.* **2016**, *7*, 592. [CrossRef]
62. Cangui-Panchi, S.P.; Ñacato-Toapanta, A.L.; Enríquez-Martínez, L.J.; Reyes, J.; Garzon-Chavez, D.; Machado, A. Biofilm-forming microorganisms causing hospital-acquired infections from intravenous catheter: A systematic review. *Curr. Res. Microb. Sci.* **2022**, *3*, 100175. [CrossRef] [PubMed]
63. Bonadonna, L.; Briancesco, R.; Coccia, A.M. Analysis of Microorganisms in Hospital Environments and Potential Risks. In *Indoor Air Quality in Healthcare Facilities*; Capolongo, S., Settimo, G., Gola, M., Eds.; Springer International Publishing: Cham, Switzerland, 2017; pp. 53–62. [CrossRef]
64. INORGANIC STRUCTURE CRYSTAL DATABASE (ICSD). Available online: <https://icsd.products.fiz-karlsruhe.de/> (accessed on 30 May 2024).
65. Boanini, E.; Gazzano, M.; Nervi, C.; Chierotti, M.R.; Rubini, K.; Gobetto, R.; Bigi, A. Strontium and Zinc Substitution in  $\beta$ -Tricalcium Phosphate: An X-ray Diffraction, Solid State NMR and ATR-FTIR Study. *J. Funct. Biomater.* **2019**, *10*, 20. [CrossRef] [PubMed]
66. Xidaki, D.; Agrafioti, P.; Diomatari, D.; Kaminari, A.; Tsalavoutas-Psarras, E.; Alexiou, P.; Psycharis, V.; Tsilibary, E.C.; Silvestros, S.; Sagnou, M. Synthesis of Hydroxyapatite,  $\beta$ -Tricalcium Phosphate and Biphasic Calcium Phosphate Particles to Act as Local Delivery Carriers of Curcumin: Loading, Release and In Vitro Studies. *Materials* **2018**, *11*, 595. [CrossRef]
67. Habelitz, S.; Pascual, L.; Durán, A. Transformation of tricalcium phosphate into apatite by ammonia treatment. *J. Mater. Sci.* **2001**, *36*, 4131–4135. [CrossRef]

**Disclaimer/Publisher’s Note:** The statements, opinions and data contained in all publications are solely those of the individual author(s) and contributor(s) and not of MDPI and/or the editor(s). MDPI and/or the editor(s) disclaim responsibility for any injury to people or property resulting from any ideas, methods, instructions or products referred to in the content.